Astronomy & Astrophysics manuscript no. paper1-lang
May 13, 2009

© ESO 2009

arXiv:0903.1369v2 [astro-ph.GA] 13 May 2009

ATLASGAL - The APEX Telescope Large Area Survey of the Galaxy at 870 μm

F. Schuller[1], K. M. Menten[1], Y. Contreras[1,2], F. Wyrowski[1], P. Schilke[1], L. Bronfman[2], T. Henning[3], C. M. Walmsley[4], H. Beuther[3], S. Bontemps[5], R. Cesaroni[4], L. Deharveng[6], G. Garay[2], F. Herpin[5], B. Lefloch[7], H. Linz[3], D. Mardones[2], V. Minier[8], S. Molinari[9], F. Motte[8], L.-Å. Nyman[10], V. Reveret[10], C. Risacher[10], D. Russeil[6], N. Schneider[8], L. Testi[11], T. Troost[1], T. Vasyunina[3], M. Wienen[1], A. Zavagno[6], A. Kovacs[1], E. Kreysa[1], G. Siringo[1], and A. Weiß[1]

[1] Max-Planck-Institut für Radioastronomie, Auf dem Hügel 69, D-53121 Bonn, Germany
e-mail: `schuller@mpifr-bonn.mpg.de`
[2] Departamento de Astronomía, Universidad de Chile, Casilla 36-D, Santiago, Chile
[3] Max-Planck-Institut für Astronomie, Königstuhl 17, D-69117 Heidelberg, Germany
[4] Osservatorio Astrofisico di Arcetri, Largo E. Fermi, 5, I-50125 Firenze, Italy
[5] Laboratoire d'Astrophyisique de Bordeaux - UMR 5804, CNRS - Université Bordeaux 1, BP 89, F-33270 Floirac, France
[6] Laboratoire d'Astrophysique de Marseille - UMR 6110, CNRS - Université de Provence, F-13388, Marseille Cedex 13, France
[7] Laboratoire d'Astrophysique de l'Observatoire de Grenoble, BP 53, F-38041 Grenoble Cedex 9, France
[8] Laboratoire AIM, CEA/IRFU - CNRS - Université Paris Diderot, Service d'Astrophysique, F-91191 Gif-sur-Yvette, France
[9] Istituto Fisica Spazio Interplanetario - INAF, Via Fosso del Cavaliere 100, I-00133 Roma, Italy
[10] ESO, Alonso de Cordova 3107, Casilla 19001, Santiago 19, Chile
[11] ESO, Karl Schwarzschild-Strasse 2, D-85748 Garching bei München, Germany

Received 23 December 2008; accepted 2 March 2009

ABSTRACT

Context. Thanks to its excellent 5100 m high site in Chajnantor, the Atacama Pathfinder Experiment (APEX) systematically explores the southern sky at submillimeter wavelengths, in both continuum and spectral line emission. Studying continuum emission from interstellar dust is essential to locating the highest density regions in the interstellar medium, and deriving their masses, column densities, density structures, and large-scale morphologies. In particular, the early stages of (massive) star formation remain poorly understood, mainly because only small samples of high-mass proto-stellar or young stellar objects have been studied in detail so far.
Aims. Our goal is to produce a large-scale, systematic database of massive pre- and proto-stellar clumps in the Galaxy, to understand how and under what conditions star formation takes place. Only a systematic survey of the Galactic Plane can provide the statistical basis for unbiased studies. A well characterized sample of Galactic star-forming sites will deliver an evolutionary sequence and a mass function of high-mass, star-forming clumps. This systematic survey at submillimeter wavelengths also represents a preparatory work for Herschel and ALMA.
Methods. The APEX telescope is ideally located to observe the inner Milky Way. The Large APEX Bolometer Camera (LABOCA) is a 295-element bolometer array observing at 870 μm, with a beam size of $19\farcs2$. Taking advantage of its large field of view ($11\farcm4$) and excellent sensitivity, we started an unbiased survey of the entire Galactic Plane accessible to APEX, with a typical noise level of 50–70 mJy/beam: the APEX Telescope Large Area Survey of the Galaxy (ATLASGAL).
Results. As a first step, we covered $\sim$95 deg^2 of the Galactic Plane. These data reveal $\sim$6000 compact sources brighter than 0.25 Jy, or 63 sources per square degree, as well as extended structures, many of them filamentary. About two thirds of the compact sources have no bright infrared counterpart, and some of them are likely to correspond to the precursors of (high-mass) proto-stars or proto-clusters. Other compact sources harbor hot cores, compact Hɪɪ regions, or young embedded clusters, thus tracing more evolved stages after massive stars have formed. Assuming a typical distance of 5 kpc, most sources are clumps smaller than 1 pc with masses from a few 10 to a few 100 $M_\odot$. In this first introductory paper, we show preliminary results from these ongoing observations, and discuss the mid- and long-term perspectives of the survey.

Key words. Surveys — Submillimeter — ISM: structure — Dust, extinction — Stars: formation — Galaxy: disk

1. Introduction

Dust continuum emission in the (sub)millimeter (submm) range is one of the most reliable tracers of the earliest phases of star formation since it directly probes the dense interstellar material from which the stars form. Trying to understand the formation and early evolution of stars is an important field of modern astrophysics (see the review of McKee & Ostriker 2007, and references therein).

A large amount of theoretical effort has been aimed at constraining the early stages of the formation of isolated low mass (solar-like) stars, although two quite different pictures are being maintained. On the one hand, a collapse picture has emerged whose "long" timescales are determined by ambipolar diffusion (Shu et al. 1987; Adams et al. 1987). On the other, a scenario is advocated in which the star formation rate is governed by supersonic turbulence (Mac Low & Klessen 2004). Many observational campaigns have contributed crucial data and in particular systematic (sub)millimeter surveys of nearby star-forming

---

Send offprint requests to: F. Schuller regions, such as Chamaeleon, Perseus, and Ophiuchus, have resulted in the detection of many prestellar and proto-stellar condensations (André et al. 2000; Ward-Thompson et al. 2007). They have allowed determination of the dense core mass spectrum down to substellar masses, and investigation of its relationship to the initial mass function (Motte et al. 1998; Gahm et al. 2002; Hatchell et al. 2005).

High-mass star formation is even less well constrained (e.g., Zinnecker & Yorke 2007; Beuther et al. 2007, for reviews) and there is controversy about how these stars attain their final masses: either driven by turbulence (McKee & Tan 2003) or competitive accretion (e.g., Bonnell et al. 2004). Since high-mass stars seem to form mostly in clusters (along with many more lower-mass stars), it is fundamental to have a good estimate of the mass distribution of cluster-forming clumps in the Giant Molecular Clouds (GMCs) they are part of. This is exactly one of the major goals of the present effort.

A cardinal reason for the many open questions concerning high-mass star formation is that the relevant timescales are short (McKee & Tan 2002), implying low number statistics in finding stars in a given evolutionary state. Moreover, high-mass stars are rare. This implies that regions in which they form are generally at large distances, which leads to the basic problem that there objects are difficult to identify. For instance, little is known about the Galactic molecular ring, a few kpc distant from us, where most of the star formation is presently taking place (e.g., Bronfman et al. 2000).

While various samples of high-mass proto-stellar objects have been defined based on various criteria, such as maser emission (e.g., Walsh et al. 1997; Pestalozzi et al. 2005) and infrared (IR) colors (Palla et al. 1991; Molinari et al. 1996; Sridharan et al. 2002; Lumsden et al. 2002; Robitaille et al. 2008), an *unbiased* sample has not yet been assembled. Much effort has focused on follow-up studies of bright IR sources detected by the Infrared Astronomy Satellite (IRAS) and showing far-infrared (FIR) colors typical of ultra-compact Hii regions (Wood & Churchwell 1989), e.g., in high-density molecular tracers (Bronfman et al. 1996; Molinari et al. 1996), dust continuum emission (Faúndez et al. 2004), or maser emission (e.g., Palla et al. 1993; Beuther et al. 2002). While some studies have revealed a few massive cold cores in the neighborhood of the central compact Hii region (e.g., Garay et al. 2004), they were mostly biased against the earliest, possibly coldest phases of massive star formation.

Alternatively, dense condensations in Infrared Dark Clouds (IRDCs, see Simon et al. 2006, for a compilation) are promising hunting grounds for the initial stages of high-mass star formation (e.g., Rathborne et al. 2006; see also the reviews by Menten et al. 2005; Wyrowski 2008). IRDCs appear in absorption by dust even at mid-infrared wavelengths against the diffuse emission of the Galactic Plane and trace high column densities. However, IRDCs become increasingly difficult to identify the further away they are, and the relative contributions by foreground and background emission may be difficult to estimate. Moreover, not all massive dust condensations appear as infrared dark clouds. For example, the two most massive condensations (with masses of 200 and 800 $M_\odot$ at a distance of 1.3 kpc) observed at 870 μm in the photo-dissociation region (PDR) bordering the RCW 120 Hii region (Deharveng et al. 2009) are not detected as IRDCs at 8 or 24 μm. They are hidden, at these wavelengths, by the bright emission of the adjacent foreground PDR.

Cold dust absorbing the IR radiation also shows thermal emission in the submm regime. This grey body emission is generally optically thin and, thus, an excellent tracer of the dust mass and, by inference, total mass of the emitting cloud. Therefore, observations in the submm continuum are complementary to the IR extinction techniques. Given the short timescales for the formation of high-mass stars, all early formation stages will still be associated with strong dust continuum emission, allowing a systematic study of a large range of evolutionary phases.

Several groups have performed large-scale mapping of molecular complexes in the (sub)millimeter continuum. Using the Submillimetre Common User Bolometer Array (SCUBA) instrument, Johnstone et al. (2004) mapped 4 deg^2 of the Ophiuchus star-forming cloud, and Hatchell et al. (2005) covered 3 deg^2 of the Perseus molecular cloud. Complementary to the Spitzer “Cores to Disks” legacy project (Evans et al. 2003), Enoch et al. (2006) mapped 7.5 deg^2 covering the Perseus cloud, and Young et al. (2006) mapped nearly 11 deg^2 covering Ophiuchus, both using the BOLOCAM instrument at 1.1 mm.

In the field of high-mass star formation, Moore et al. (2007) covered 0.9 deg^2 of the W3 giant molecular cloud with SCUBA. Going to larger scales, Motte et al. (2007) used the MAMBO instrument to obtain a complete dust-continuum map of the molecular complex associated with the Cygnus X region. From this 3 deg^2 map, they could derive some statistically significant results about the characteristics (e.g., mass, density, outflow power, mid-IR flux) and lifetimes of different evolutionary phases of high-mass star formation. In particular, no high-mass analog of pre-stellar dense cores was found by this study, hinting at a short lifetime for the earliest phases of dense cores in which high-mass stars are being formed. An unbiased survey of the complete Galactic Plane will allow us to place far stronger constraints on this stage of high-mass star formation.

On an excellent 5100 m high site and at a latitude of $-23°$, the 12 m diameter APEX telescope (Güsten et al. 2006a,b) is ideally located to make sensitive observations of the two inner quadrants of the Galactic Plane. A consortium led by the Max Planck Institute für Radioastronomie (MPIfR) in Bonn, involving scientists from the Max Planck Institute für Astronomie in Heidelberg and from the ESO and Chilean communities has embarked on the APEX Telescope Large Area Survey of the Galaxy (ATLASGAL). This project aims at a systematic survey of the inner Galactic Plane, mapping several 100 deg^2 with a uniform sensitivity. In this paper, we present the first data taken and analyzed. The observing strategy and data reduction are described in Sect. 2 and Sect. 3. First preliminary results are discussed in Sect. 4. Finally, we discuss longer term perspectives in Sect. 5.

2. Observations

Observations of continuum emission from interstellar dust at (sub)millimeter wavelengths are completed most effectively with sensitive broadband bolometer detectors. Modern (sub)millimeter bolometer development started in the mid 1980s with single-pixel-element instruments, with a resolution, i.e., diffraction-limited FWHM beam size, of 11$''$ for the IRAM 30 m telescope at 1.2 mm and 19$''$ for the James Clerk Maxwell Telescope (JCMT) at 1.1 mm. Since then, arrays with more and more elements have been developed and deployed to telescopes. Modern arrays of bolometers have hundreds of elements: 384 for the Nyquist-sampled Submillimeter High-Angular Resolution Camera 2 (SHARC II, Dowell et al. 2003), and 295 for the Large APEX Bolometer Camera (LABOCA), which was recently deployed at the APEX telescope (Siringo et al. 2007, 2009). With a field of view of 11$'\!.$4, and a single-pixel sensitivity (noise equivalent flux density, NEFD) in the range 40–70 mJy s$^{1/2}$, LABOCA

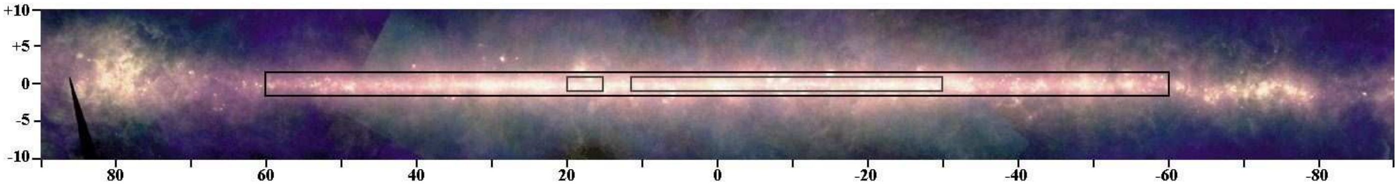

Fig. 1. Coverage of the ATLASGAL observations overlaid on an IRAS false color image (12 μm in blue, 60 μm in green and 100 μm in red). This image covers ±90° in galactic longitude, and ±10° in latitude. The long frame shows the area that we plan to cover until the end of 2009: ±60° in *l* and ±1.5° in *b*. The smaller frames inside delineate the area that was observed in 2007 (see also Fig. 3).

is the most powerful bolometer array for large-scale mapping operational on a ground-based telescope.

The ATLASGAL observations are carried out at the APEX 12 m submm antenna, which is a modified copy of the VERTEX prototype antenna for the Atacama Large Millimeter Array (ALMA). The antenna has a surface accuracy of 15 μm rms, i.e., higher than ALMA specifications. Two additional Nasmyth cabins allow several receivers to be ready for use. The LABOCA instrument is an array of 295 bolometers arranged in an hexagonal pattern, with two-beam spacing between bolometers (Siringo et al. 2009). It is located at the Cassegrain focus, where it has an effective field of view of 11.′4 in diameter. Small variations in the beam shape are seen within the field of view, but should not affect the data (see Siringo et al. 2009, for a discussion of these effets). Its bandpass is centered on 870 μm (frequency 345 GHz) with a bandwidth of 60 GHz. The beam at this wavelength was measured to have a width of 19.″2 FWHM. The number of usable bolometers at the end of the reduction, after flagging the noisy ones and the ones that do not respond (Sect. 3) is usually between 250 and 260.

In the present paper, we focus on the data acquired in 2007, which cover 95 deg^2: $-30° \leq l \leq +11.5°$ and $+15° \leq l \leq +21°$, with $|b| \leq 1°$ (Fig. 1), at a one-σ sensitivity of 50 to 70 mJy/beam. For comparison, the 9-year lifetime of the SCUBA instrument resulted in a total of 29.3 deg^2 mapped at 850 μm (Di Francesco et al. 2008). A single observation consists in an on-the-fly map, 2° long and 1° wide, with 1.′5 steps between individual lines, resulting in fully sampled maps covering 2 deg^2. The scanning speed used is 3′/s. This fast scanning allows us to perform observations in total power mode, i.e., without chopping. Each map crosses the Galactic Plane with a ±15° position angle with respect to the Galactic latitude axis. Two consecutive maps are spaced by 0.5° along the Galactic Plane, with a 30° difference in position angle (Fig. 2). Thus, each position on the sky is observed in two independent maps, of different position angles, greatly reducing many systematic effects (e.g., striping in the scanning direction).

In the longer term, we plan to extend the coverage to ±60° in longitude and ±1.5° in latitude (Fig. 1), with the same sensitivity of 50 mJy/beam. An ESO large programme was approved to conduct these observations, which will require a total of 430 hours, including all overheads, to cover 360 deg^2. The observing time will be shared between 45 hours from Chile, 225 hours from the Max-Planck-Society (MPG), and 160 hours from ESO, spanning four semesters in 2008–2009.

3. Data reduction and source extraction

The raw data are recorded in MB-FITS (Multi-Beam FITS) format by the FITS writer, which is part of the APEX Control System (APECS, Muders et al. 2006). These data were processed using the BOlometer array data Analysis package (BOA; Schuller et al. in prep.), which was specifically developed as part of the LABOCA project to reduce data obtained with bolometers at the APEX telescope. The reduction steps involved in the processing of the ATLASGAL data are described in the next subsections.

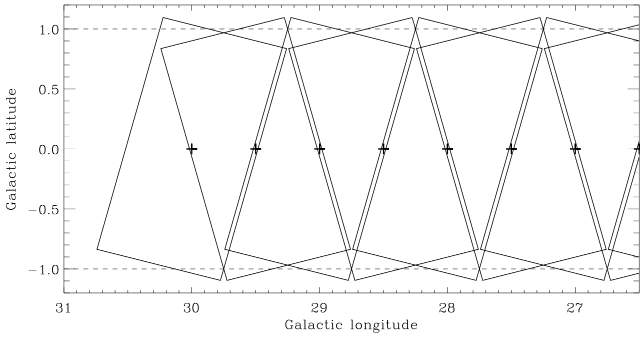

Fig. 2. Mapping strategy: each rectangular frame represents a single map. The plus symbols show the maps centers. A position angle of 15° with respect to the Galactic axis was chosen. Two neighboring maps are observed with position angles of +15° and −15°, respectively.

3.1. First step: from raw data to 2 deg^2 maps

Each single observation is processed and calibrated to compile a map covering 2 deg^2. The data are calibrated by applying an opacity correction, as determined from skydips observed typically every two hours (see Siringo et al. 2009, for more details). In addition, the flux calibration is regularly (every hour) checked against primary calibrators (the planets Mars, Neptune and Uranus) or secondary calibrators (bright Galactic sources, for which the fluxes at 870 μm were measured during the commissioning of LABOCA). If any discrepancy is found between the opacity-corrected flux of a calibrator and its expected flux, then the correction factor required to obtain the expected flux is also applied to the science data. Given the uncertainties in the fluxes of the planets themselves, we estimate that, altogether, the typical calibration error should be lower than 15%. Pointing scans are also completed using bright sources every hour; the pointing rms is typically of order 4″.

The reduction steps are as follows:

- flagging bad pixels (those that do not respond, or do not see the sky)
- correlated noise removal (see below for details)
- flagging noisy pixels
- despiking
- low-frequency filtering (see below)

- first-order baseline on the entire timestream
- building a map, using natural weighting: each data point has a weight 1/rms^2, where rms is the standard deviation of each pixel

The main source of noise in the submm is variable atmospheric emission (sky noise), which varies slowly with typical amplitudes of several 100 Jy. Fortunately, this sky noise is highly correlated between bolometers. For each integration, the correlated noise is computed as the median value of all normalized signals. It is removed in successive steps: as a first step, the median for all bolometers is computed, and then the median for all pixels connected to the same amplifier box (groups of 60 to 80 pixels); finally, the correlated signal is computed for groups of 20 to 25 pixels sharing the same read-out cable. A consequence of this processing is that uniformly extended emission is filtered out, since there is no way of distinguishing extended astronomical signal observable by all bolometers from correlated (e.g., atmospheric) noise. The strongest effect occurs when computing the correlated noise in groups of pixels: these groups typically cover $\sim 1\farcm5 \times 5'$ on the array, and since the correlated noise is computed as the median value of the signals, any emission that is seen by more than half the bolometers in a given group is subtracted. Thus, *uniform* emission on scales larger than $\sim 2\farcm5$ is filtered out.

Another low-frequency filtering is performed, to reduce the effects of the slow instrumental drifts, which are uncorrelated between bolometers. This filtering is performed in the Fourier domain, and applies to frequencies below 0.2 Hz, which, given the scanning speed of 3′/s, translates to spatial scales of above 15′, i.e., larger than the LABOCA field of view. Therefore, this step should not affect extended emission that has not already been filtered-out by the correlated noise removal.

This reduction is optimized for recovering compact sources with high signal-to-noise ratio. Alternatively, the data can be reduced without subtracting all components of correlated noise, which allows one to recover more extended emission, but results in an increased noise level in the final maps.

3.2. Second step: using a source model

The data processed in the first step are then combined into groups of three maps: for each position l_0, the maps centered on l_0, $l_0 + 0.5°$, and $l_0 - 0.5°$ are computed and coadded to obtain a two-fold coverage of the central 1×2 deg^2 area (see Fig. 2). This combined map is then used as a source model for masking in the timestreams the data that correspond to positions in the map where the emission is above some given threshold. The full reduction is then performed again, involving the same processing steps as described in the previous section with less conservative parameters for despiking and correlated-noise removal. During this step, datapoints corresponding to strong emission in the model map are masked for the various computations (baseline removal, despiking, subtraction of correlated noise), but the results of these computations are also applied to the masked data.

Finally, another iteration is performed, this time *subtracting* the source model (resulting from the previous step) from the raw data. In this case, all datapoints are used in the computations, and processing steps that may affect strong sources (e.g., despiking) can be performed almost without caution, since most of the true emission has been subtracted from the signals. Before adding the source model back into the reduced data, weights are computed using sliding windows along the timestreams. The weight applied to each datapoint is 1/rms^2, where rms is the standard deviation in a given pixel computed for 50 datapoints.

The net effect of these iterations with a source model is to reduce the negative artifacts appearing around strong sources in the first reduction step and to recover some fraction of the flux of bright objects lost in that step. The final flux uncertainty for compact sources should be lower than 15% (Sect. 3.1), as also confirmed by hundreds of measurements of primary and secondary calibrators (Siringo et al. 2009).

When compiling maps with two pixels per beam, the final noise level obtained from individual observations is generally in the 70–100 mJy/beam range. In the combined maps, the rms is then 50–70 mJy/beam in overlapping regions. The combined maps covering continuously −30° to +12° in longitude are shown in Fig. 3, and example zooms are shown in Fig. 4.

3.3. Compact source extraction

A preliminary extraction of compact sources was completed using the SExtractor programme (Bertin & Arnouts 1996). The extraction was performed in two steps: first, the peaks were detected on signal-to-noise ratio maps; SExtractor was then used to compute the source peak positions and fluxes, as well as their sizes. Since we were only interested in compact sources when compiling this first catalog, one constraint used was that the ratio of major to minor axes should be lower than 4. Details of the method and the complete catalog itself will be published in a forthcoming paper (Contreras et al. in prep).

This source extraction resulted in ∼6000 objects with peak fluxes above 250 mJy/beam, over the 95 deg^2 mapped. The average source density is thus 63 sources per square degree, but the source distribution is highly non-uniform (Fig. 5). The source sizes range from one LABOCA beam size (19″) to about 8 beam widths (150″). We note that the filtering of uniform emission on spatial scales larger than $2\farcm5$ (Sect. 3.1) should not prevent extraction of sources of larger FWHM, as long as they are reasonably compact, i.e., with a profile close to a Gaussian shape; their fluxes however would be severely underestimated.

Assuming a typical distance of 5 kpc, which roughly corresponds to the molecular ring, the 19″ resolution translates to ∼0.5 pc. The LABOCA data are therefore sensitive to molecular clumps, following the terminology of Williams et al. (2000, see also Motte & Hennebelle 2009), where dense cores have typical sizes of ∼0.1 pc and are embedded in pc-scale clumps, themselves being part of >10 pc GMCs. The sources distribution is strongly peaked toward the Galactic Plane, as seen in Fig. 5, and in particular in the direction of the Galactic Center, with an excess of sources toward negative latitudes. Within the central few degrees, sources exhibit an excess at positive longitudes. Other peaks in longitude are visible in Fig. 5 in the direction of the Norma arm ($-30° \leq l \leq -20°$), and around $l = -8°$, which corresponds to the NGC6334/NGC6357 star-forming complexes.

As seen in Fig. 5, the latitude distribution of compact sources peaks at $b = -0.09°$, which is significantly below zero. This effect is seen in all ranges of longitudes. We suspect that this is due to the Sun being slightly above the Galactic Plane, but this effect requires more study. The reason for the asymmetry in longitude within the few central degrees is unclear, but is certainly real, as can be seen also in Fig. 3. Interestingly, the distribution of compact sources seen with Spitzer at 24 μm shows an excess toward *negative* longitudes (Hinz et al. 2009). While no clear explanation is found, Hinz et al. (2009) suggested that this could reflect the true distribution of infrared sources near the Galactic Center, if more molecular clouds are present at positive longitudes, ob-

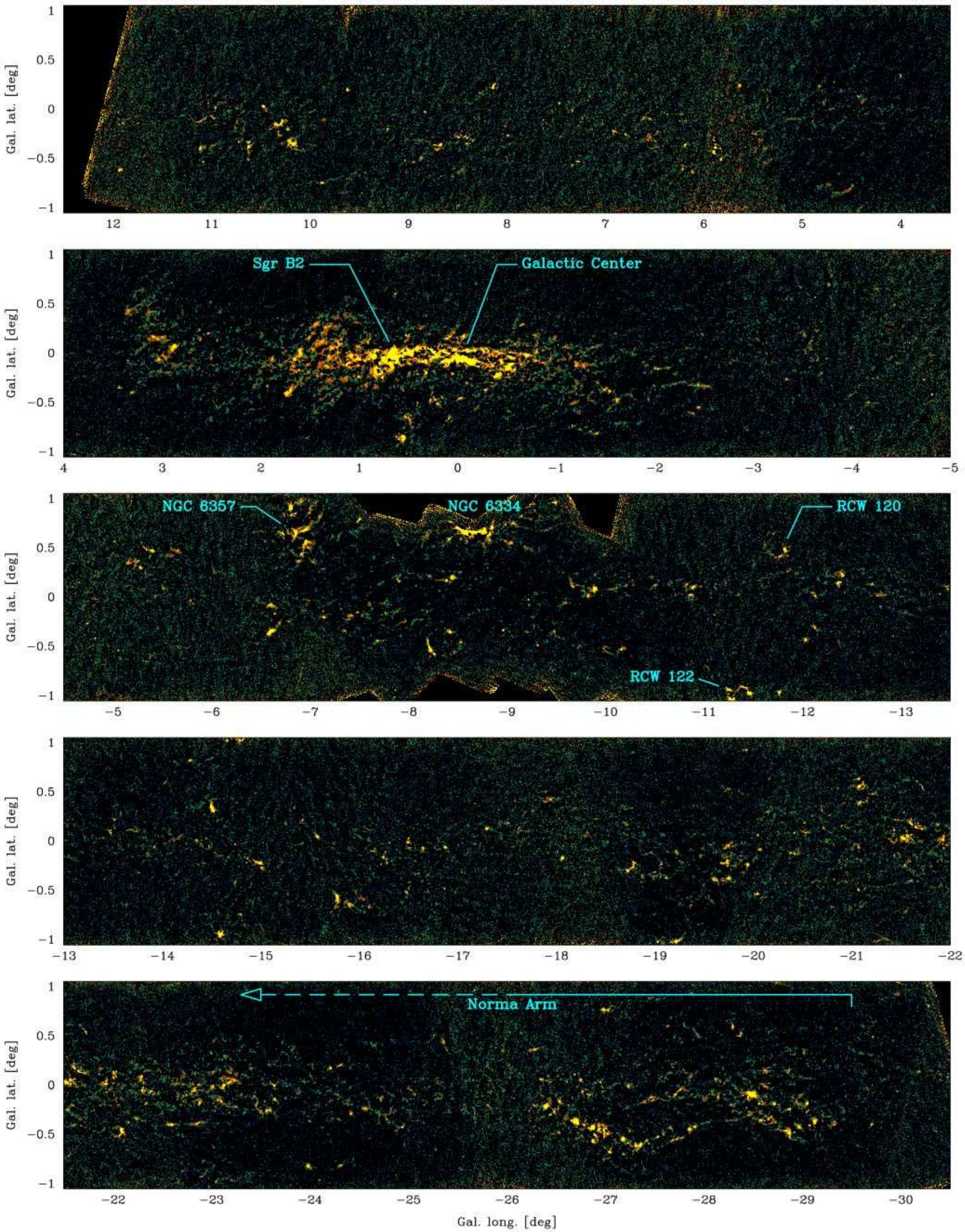

Fig. 3. Combined maps showing 84 deg^2 of the ATLASGAL data obtained in 2007, at 870 μm with a resolution of 19″. The color scale is logarithmic between 0.05 and 1.0 Jy/beam. The rms is of order 50 to 70 mJy/beam in most parts of these maps. A few known regions are labeled in the maps. See also Fig. 4.

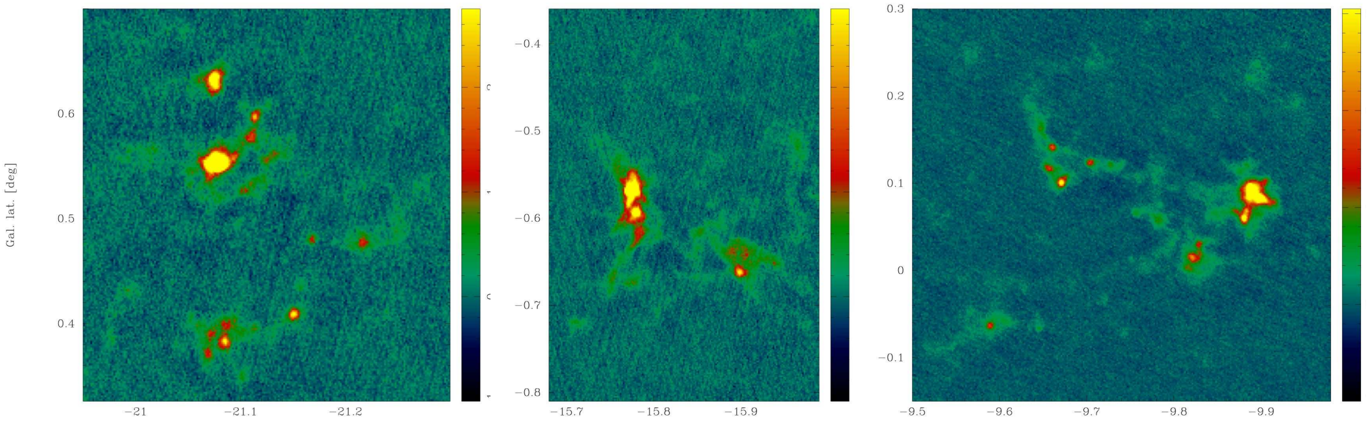

Fig. 4. Zooms into selected regions. These maps are projected with three pixels per beam, resulting in a pixel r.m.s. of between 80 and 130 mJy/beam. All maps are shown in linear scale, calibrated to Jy/beam. The color scale has been chosen to highlight the negative artifacts, but doesn't cover the full range of fluxes in these images: the brightest peaks are, from left to right, 18.6, 17.2, and 7.2 Jy/beam; the most negative pixels are at -0.49, -0.54, and -0.43 Jy/beam, respectively.

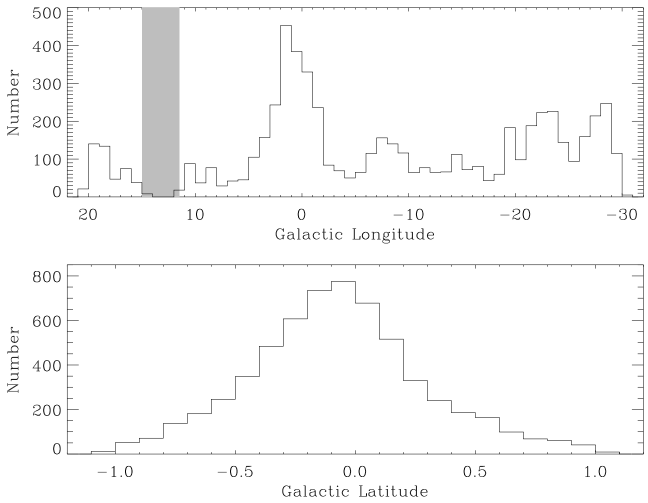

Fig. 5. Distribution of the 6000 compact sources in Galactic longitude (top, with 1° bins) and latitude (bottom, with 0.1° bins). Note that the longitude range +11.5° to +15° is not covered by the present data.

scuring the compact IR sources, which would be consistent with the distribution that we observe in the submm.

4. First results

The large scale maps in Fig. 3 clearly show a variety of submillimeter sources from bright, compact objects to faint, extended regions on the arcmin scale, and long filaments on almost a degree scale. The survey is very rich, and a wealth of new results is expected. To provide a flavor of these and to illustrate how a complete view of the Galactic star-formation activity will be achieved from ATLASGAL, we present a first analysis and some first results for a typical 1° wide slice, around *l* = 19° (Fig. 6). This region shows a reasonably rich population of sources, and is also representative of regions with several cloud complexes at different distances. We also selected this region because it is covered by the Galactic Ring Survey (GRS, Jackson et al. 2006), which provides good quality CO data that we use to discuss the association with large-scale molecular clouds.

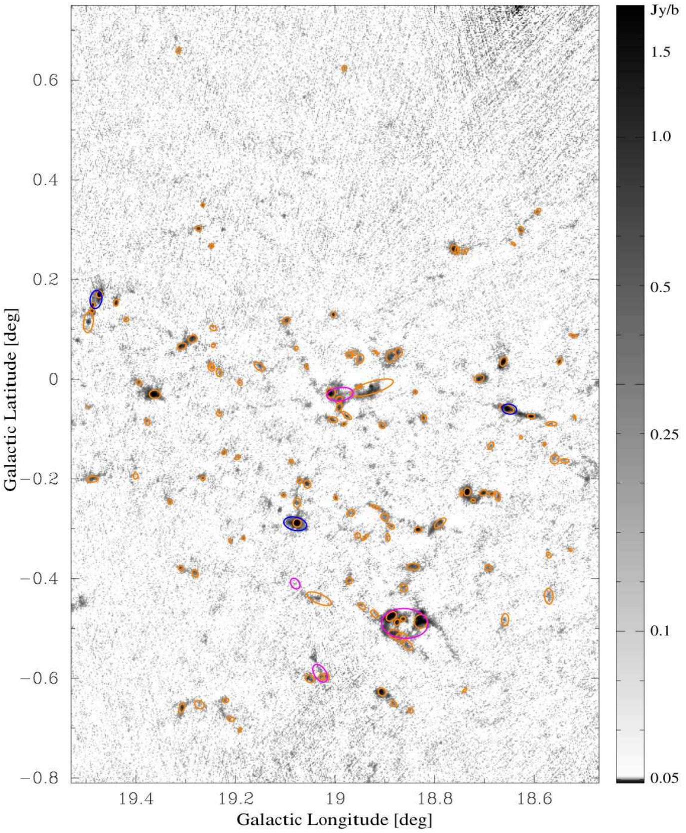

Fig. 6. Example combined map covering 1×1.5 deg^2, shown in logarithmic scale. The pixel scale is one third of the beam and the standard deviation between pixels in empty regions of the maps is typically 90 mJy/beam. The brightest peak is at 6.2 Jy/beam. The 128 compact sources extracted in this region are shown with orange ellipses, with sizes and position angles as measured with SExtractor (Sect. 3.3). Ultra-compact Hɪɪ regions discussed at the end of Sect. 4.2 are shown with blue ellipses; compact and classical Hɪɪ regions are indicated with magenta ellipses.

4.1. Compact sources and extended emission at $l = 19°$

In a number of Galactic directions, there is submillimeter emission virtually everywhere in the Galactic Plane. The region shown in Fig. 6 at $l = 19°$ is one of these. From our preliminary source extraction, we identified 128 compact sources with peak fluxes above 0.25 Jy/beam in this $1{\times}2$ deg^2 slice (no source was detected outside the $|b| \leq 0.75°$ range shown in Fig. 6), in perfect agreement with the average 63 extracted sources per square degree. Only 16 of these sources have a probable known counterpart in the SIMBAD database (infrared, millimeter or radio source within a 10″ search radius), which means that more than 80% have not yet been studied. Some of them certainly have counterparts in the new infrared surveys observed with Spitzer (see e.g., Fig. 14); associations between ATLASGAL and Spitzer data will be addressed elsewhere.

As can be seen in Fig. 6, most of the compact sources are embedded in more extended emission of a few arcmin extent. Many of these features appear filamentary and could correspond to overdensities within giant molecular clouds, in which even denser clumps are forming. That small groups of clumps belong to one single molecular complex is sometimes confirmed by information about their kinematics, as discussed in the next section.

4.2. Coherent complexes and distance determination

Toward the inner Galactic Plane, the detected sources can be at any distance. *A priori*, any direction of the Plane could contain sources at distances distributed over a significant range of values, except for some peculiar lines of sight, like the Galactic Center (GC), where most sources are probably concentrated close to the GC itself. In other directions, one expects to find overdensities of objects at particular distances, corresponding to the Galactic arms, particularly in the molecular ring region, but a wide range of distances is allowed.

Distance determination in the Galaxy is a difficult issue. The kinematic distances can be obtained from molecular-line follow-up surveys. We have started systematic observations of the compact ATLASGAL sources in NH_3 with the Effelsberg 100 m telescope (Wienen et al. in prep.) for the northern part of the plane, and in many molecular lines observed simultaneously with the MOPRA 22 m telescope (Wyrowski et al. in prep.) for the southern part. The NH_3 lines were detected for nearly all targeted sources, showing various line widths and shapes, and usually with only one velocity component (see examples in Fig. 7). This is expected since NH_3 is a high-density tracer, which is detectable only for the dense cores also seen with LABOCA.

Twenty-four of the total 278 sources observed so far in NH_3 are located in the region shown in Fig. 6. The distribution of measured V_{LSR} is shown in Fig. 8. Interestingly, the velocities are not spread over the entire permitted range, but are mostly gathered in very few coherent groups. In addition, these groups are also spatially coherent (see Fig. 8 top). We can conclude that the ATLASGAL emission is dominated by a few bright complexes at specific distances. In the $l = 19°$ region, 15 out of 24 ATLASGAL compact sources detected in NH_3 have a velocity of between 60 and 66 km s^{-1}. This complex would be at a distance of 4 or 12 kpc depending on whether the near or far solution for the kinematic distance is correct. In addition to this clear velocity component, two sources are at rather low velocities of around 20 km s^{-1}, a few are between 35 and 50 km s^{-1}, and two are at 80 and 81 km s^{-1}.

To study the spatial distribution of these velocity components in greater detail, we used the ^{13}CO(1–0) data from the GRS to identify the molecular complexes associated with these velocities (Fig. 9). In addition, using an extinction map obtained from the 2MASS catalog (Bontemps, priv. com.), it is possible to recognize that some of these complexes account for the detected extinction and are therefore most probably at their near kinematic distance. This is the case for the 36 to 52 km s^{-1} complex, and for a small part of the ∼20 km s^{-1} clouds (dashed-line arc around (19.35, 0.05) in Fig. 9). The main complex at 65 km s^{-1} is more complicated: parts of this complex are associated with peaks of extinction, but other parts correspond to very low extinction. Nevertheless, this might indicate that it is also at the near distance. In addition, this complex appears quite extended at 8 μm and 870 μm, which again favors the near distance solution. The full extent of the ^{13}CO emission, spanning about 0.9° in latitude, corresponds to 70 pc at a distance of 4.5 kpc, typical of GMC dimensions.

Finally, we note that a large part of the ∼20 km s^{-1} component is a string of compact CO clouds that are not associated with any feature in the extinction map. They are therefore most probably complexes at their far distance, i.e., on the order 14 kpc. The source at $(l, b) = (18.76, 0.26)$ coincides with a very compact object in the GLIMPSE (Benjamin et al. 2003) image (Fig. 10), which is also consistent with a far distance solution.

Additional constraints can be obtained from absorption lines toward Hɪɪ regions (e.g., Sewilo et al. 2004; Anderson & Bania 2009). Anderson & Bania (2009) presented seven Hɪɪ regions with measured distances determination in the range $18.5° \leq l \leq 19.5°$: three ultra-compact and four compact/classical regions. All three ultra-compact and three out of the four com-

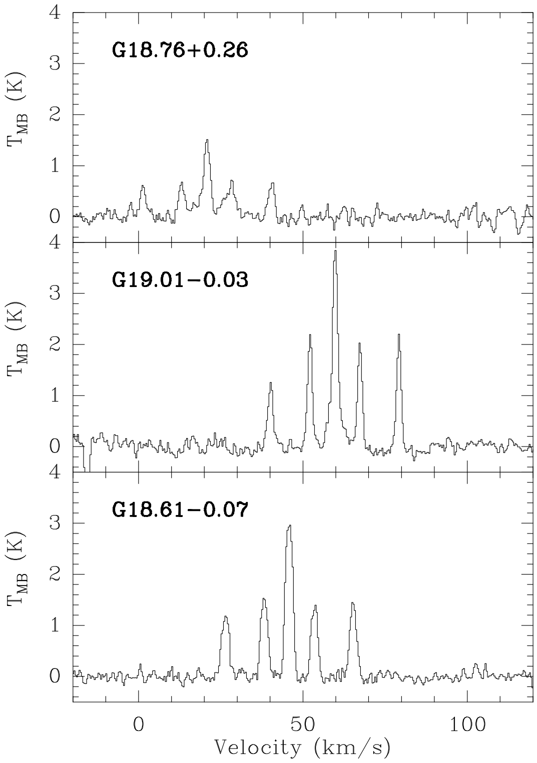

Fig. 7. Example spectra in NH_3 (1,1) transition for three sources located in the region shown in Fig. 6. G18.76+0.26 is probably at a distance of ∼14 kpc, while G19.01-0.03 and G18.61-0.07 are probably at 4.3 and 3.7 kpc, respectively.

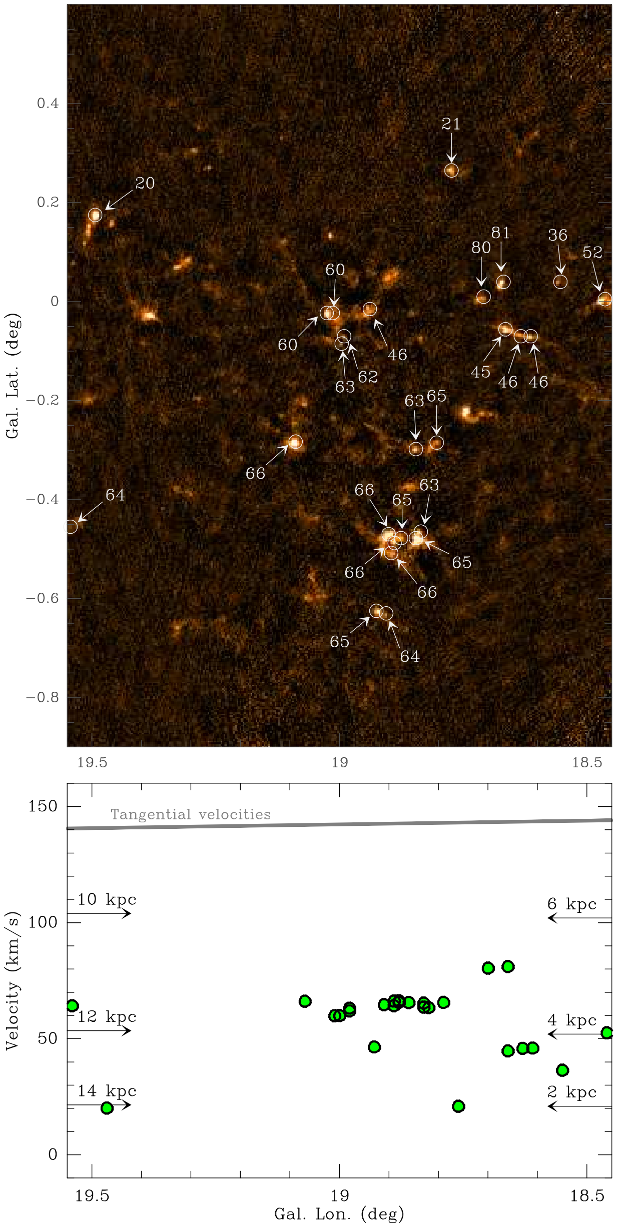

Fig. 8. *Top*: LSR velocities (in km s^{-1}) derived from NH$_3$ spectra are indicated next to the sources visible in the ATLASGAL map. *Bottom*: the measured LSR velocities are plotted against Galactic longitude. Kinematic distances derived using the Galactic rotation model of Brand & Blitz (1993) are indicated on the right for the near distance solution, and on the left for the far solution. The thick line near 140 km s^{-1} shows the maximal expected velocity, which corresponds to the tangential point for a circular orbit with a radius ~2.7 kpc around the GC.

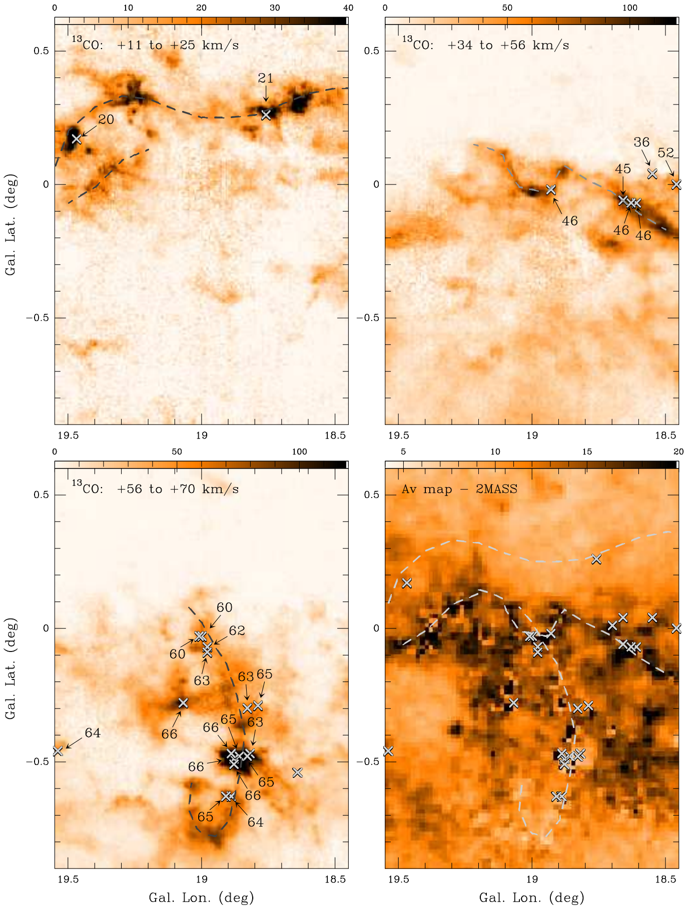

Fig. 9. Integrated ^{13}CO(1–0) intensity over different ranges of velocities, shown in the top-left corner of each panel, from the GRS data. The color scale is shown on top of each panel, in units of K km s^{-1}. LSR velocities of ATLASGAL sources derived from the NH$_3$ spectra are indicated. *Bottom right*: extinction map derived from the 2MASS catalog. The color scale corresponds to magnitudes of visual extinction. In all panels, dashed lines outline structures that seem connected together.

pact regions have clear counterparts in ATLASGAL (Fig. 6). Except for C18.95-0.02, which exhibits several components in the ^{13}CO spectrum, and C19.04-0.43, which we did not observe in NH$_3$, there is good agreement between the LSR velocities derived from radio recombination lines, from ^{13}CO(1–0) and from NH$_3$ transitions. Finally, results from, both, Sewilo et al. (2004) and Anderson & Bania (2009) generally agree with our conclusions for the objects located in the test field, the +65 km s^{-1} complex being at the near distance and the +20 km s^{-1} clump G19.47+0.17 being at the far distance. However, in a few cases, the correct interpretation of absorption lines remains difficult: Sewilo et al. (2004) and Anderson & Bania (2009) concluded with a far distance solution for U18.66-0.06, but all three ATLASGAL sources that we observed in NH$_3$ (with $v_{\rm LSR} \sim +45$ km s^{-1}) follow an IRDC clearly detected by GLIMPSE (Figs. 10 and 14), which favors a near distance. Discussion of all individual sources goes beyond the scope of the present paper, and will be addressed elsewhere.

4.3. Mass estimates

Dust emission is generally optically thin in the submm continuum. Therefore, following Hildebrand (1983), the total mass in a core is directly proportional to the total flux density F_ν, integrated over the source:

$$M = \frac{d^2\, F_\nu\, R}{B_\nu(T_D)\, \kappa_\nu}, \qquad (1)$$

where d is the distance to the source, R is the gas-to-dust mass ratio, B_ν is the Planck function for a dust temperature T_D, and κ_ν is the dust absorption coefficient. The beam-averaged column

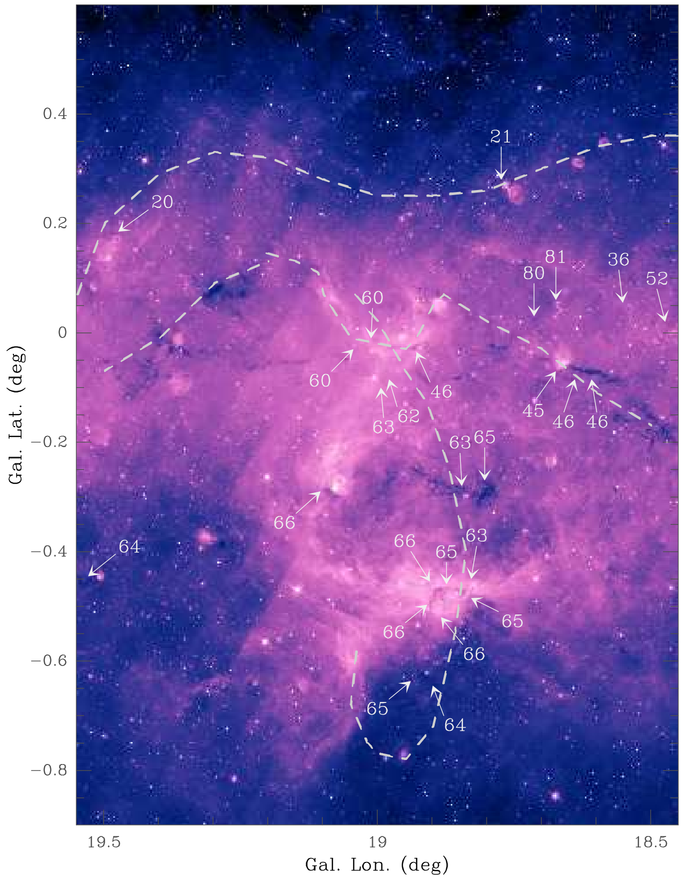

Fig. 10. 8 μm map of the region shown in Fig. 6 from the GLIMPSE survey. LSR velocities derived from NH_3 data are indicated.

density, which does not depend on the distance, can also be computed with:

$$N_{H_2} = \frac{F_\nu R}{B_\nu(T_D)\,\Omega\,\kappa_\nu\,\mu\,m_H}, \tag{2}$$

where Ω is the beam solid angle, μ is the mean molecular weight of the interstellar medium, which we assume to be equal to 2.8, and m_H is the mass of an hydrogen atom. Assuming a gas-to-dust mass ratio of 100, and $\kappa_\nu = 1.85$ cm^2 g^{-1} (interpolated to 870 μm from Table 1, Col. 5 of Ossenkopf & Henning 1994), our survey is sensitive to cold cores with typical masses in the range $\sim$100 $M_\odot$ at 8 kpc to below 1 $M_\odot$ at 500 pc (Fig. 11). The 5-σ limit of 0.25 Jy/beam corresponds to column densities in the range 3.6×10^{21} cm^{-2} for $T_D = 30$ K to 2.0×10^{22} cm^{-2} for $T_D = 10$ K, equivalent to visual extinctions of 4 mag to 21 mag, respectively (using the conversion factor from Frerking et al. 1982).

These computations assume that the emission at 870 μm is optically thin. For the brightest source detected so far (Sgr B2(N), which has a peak flux density at 170 Jy/beam), we compute the beam-averaged optical depth using:

$$\tau_{870} = -ln\left[1 - \frac{F_\nu}{\Omega B_\nu(T)}\right] \tag{3}$$

This infers an optical depth of $\tau \leq 0.31$ for a temperature $T \geq 25$ K. Therefore, the optically thin assumption should be correct, even for the brightest sources.

Using the distances as estimated in Sect. 4.2, we calculated the masses of the clumps located around $l = +19°$ (Fig. 8); the results are summarized in Table 1. In a few cases, the SExtractor program, used to extract compact sources from the full survey (Sect. 3.3), does not reliably extract sources that appear blended. Therefore, we fitted 2D-Gaussian profiles to the 24 sources observed in NH_3 to measure their fluxes and sizes, special care being taken to separate blended sources. The results of these fits were source positions, sizes (minor and major axis FWHM), and both peak and integrated fluxes.

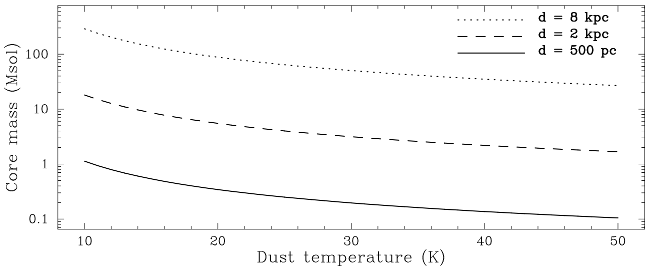

Fig. 11. Total gas plus dust masses in a core with 250 mJy integrated flux density at 870 μm (5-σ detection limit) as a function of dust temperature, for three typical distances: 500 pc (full line), 2 kpc (dashed line) and 8 kpc (dotted line).

Table 1 provides: source names (based on Galactic coordinates); equatorial coordinates and sizes, measured from Gaussian fits on the 870 μm image; LSR velocities measured with the NH_3(1,1) transition; corresponding Galactocentric radius, as well as near and far kinematic distances; peak and integrated fluxes at 870 μm; and kinetic temperatures, computed from the NH_3(1,1) and (2,2) measurements (Wienen et al., in prep.). Finally, masses for the near and far distances are computed, using the integrated 870 μm fluxes and the kinetic temperatures.

These computations assume that the 870 μm fluxes detected with LABOCA originate only in thermal emission from the dust. From spectral-line surveys, it is known that molecular lines might contribute a significant amount of flux to the emission detected by broadband bolometers. Groesbeck (1995) estimated from line surveys in the 345 GHz atmospheric window that lines can contribute up to 60% of the flux. This extreme value was found for the Orion hot core, which is peculiar due to a large contribution from wide SO_2 lines (Schilke et al. 1997). The relative contribution from CO(3–2) lines alone will only be of relevance in the case of extreme outflow sources with little dust continuum. From a quantitative analysis of the relative CO contribution in the bright massive star-forming region G327.3-0.6, observed with the APEX telescope in CO (Wyrowski et al. 2006), we found the contribution to be insignificant close to the compact hot core but to increase to 20% for the bright, extended photon-dominated region to the north of the hot core. In summary, hot molecular cores, strong outflow sources, and bright photon-dominated regions will have a flux contribution from line emission that is higher than the typical 15% calibration uncertainty (Sect. 3.1) in the continuum observations. Line follow-up observations in the mm/submm with APEX of bright sources found with ATLASGAL will help to place stronger constraints on the line flux contribution.

Another source of contamination could be free-free emission, when an HII region has already been formed. At 345 GHz the contribution from free-free should however be low compared to the thermal emission from dust. As an example, Motte et al. (2003) estimated the contribution from free-free emission at 1.3 mm in the compact fragments found within the W43 massive

Table 1. Observed and derived parameters for the 24 sources located in the region shown in Fig. 6 and observed in NH$_3$ lines. When the distance ambiguity could be solved, the preferred distance and mass are shown in boldface.

Source	RA (J2000)	Dec (J2000)	Size $''$	v_{LSR} km/s	R_G kpc	D$_{near}$ kpc	D$_{far}$ kpc	F$_{peak}$ Jy/b.	F$_{int}$ Jy	T$_{kin}$ K	N(H$_2$) $^{(1)}$	M$_{near}$ M$_\odot$	M$_{far}$ M$_\odot$
G18.55+0.04	18 24 37.85	-12 45 14.8	36×24	36.3	5.6	3.1	13.0	0.92	2.8	21.0	2.1	140	2380
G18.61–0.07	18 25 08.42	-12 45 21.6	38×26	45.8	5.2	**3.7**	12.5	1.70	5.7	32.7$^{(2)}$	2.2	**210**	2490
G18.63–0.07	18 25 09.84	-12 44 07.5	53×21	45.7	5.2	**3.6**	12.5	0.96	3.6	14.7	3.9	**420**	5010
G18.65–0.06	18 25 10.63	-12 42 24.1	43×25	44.6	5.2	**3.7**	12.5	2.25	8.1	18.3	6.4	**680**	7940
G18.66+0.04	18 24 50.98	-12 39 20.8	36×24	80.9	4.0	5.2	10.9	2.10	6.3	22.4	4.5	780	3510
G18.70+0.00	18 25 02.38	-12 38 12.6	46×34	80.3	4.0	5.1	11.0	0.84	4.5	14.8	3.4	1030	4770
G18.76+0.26	18 24 13.27	-12 27 44.6	59×42	20.8	6.6	2.0	**14.1**	1.14	9.7	15.8	4.1	320	**15090**
G18.79–0.29	18 26 15.53	-12 41 36.2	40×34	65.5	4.4	**4.5**	11.6	0.94	4.3	14.4	4.0	**830**	5360
G18.83–0.30	18 26 23.70	-12 39 38.9	37×28	63.5	4.6	**4.4**	11.7	1.35	4.8	-$^{(3)}$	5.3	**800**	5610
G18.83–0.47	18 26 59.34	-12 44 46.5	34×32	63.3	4.5	**4.5**	11.6	1.50	5.7	18.9	4.1	**680**	4600
G18.83–0.49	18 27 03.57	-12 45 06.5	58×25	65.2	4.5	**4.5**	11.6	1.34	6.7	20.8	3.2	**720**	4640
G18.86–0.48	18 27 06.20	-12 43 09.3	38×23	65.4	4.4	**4.6**	11.5	0.73	2.1	18.8	2.0	**270**	1710
G18.88–0.49	18 27 09.21	-12 42 35.1	38×25	65.5	4.5	**4.5**	11.6	1.11	3.5	22.4	2.4	**340**	2210
G18.88–0.51	18 27 15.13	-12 42 54.6	52×29	66.2	4.4	**4.6**	11.5	0.62	3.2	23.6	1.2	**290**	1840
G18.89–0.47	18 27 07.82	-12 41 38.0	64×34	66.1	4.4	**4.6**	11.5	3.39	25.4	25.9	5.9	**2040**	12840
G18.89–0.64	18 27 43.46	-12 45 48.5	28×22	64.1	4.5	**4.5**	11.6	0.58	1.2	20.0	1.5	**130**	880
G18.91–0.63	18 27 43.55	-12 44 51.0	50×43	64.5	4.5	**4.5**	11.6	1.51	11.1	17.1	4.8	**1560**	10340
G18.93–0.01	18 25 32.35	-12 26 41.4	27×25	46.3	5.1	3.7	12.4	1.33	3.1	29.3	2.0	140	1530
G18.98–0.07	18 25 51.06	-12 25 42.5	26×18	61.8	4.6	**4.4**	11.7	0.82	1.3	20.4	2.0	**140**	960
G18.98–0.09	18 25 55.22	-12 25 50.3	30×19	63.0	4.5	**4.4**	11.6	0.64	1.3	20.7	1.5	**130**	900
G18.99–0.04	18 25 45.44	-12 23 54.0	38×32	59.8	4.7	**4.3**	11.8	0.31	1.3	20.7	0.7	**120**	930
G19.01–0.03	18 25 44.61	-12 22 42.0	40×34	59.8	4.7	**4.3**	11.8	2.18	10.1	19.5	5.7	**1070**	8000
G19.08–0.29	18 26 48.77	-12 26 20.7	39×37	66.0	4.6	**4.3**	11.7	4.28	21.4	24.2	8.2	**1700**	12330
G19.47+0.17	18 25 54.50	-11 52 34.4	33×24	20.0	6.6	2.0	**14.0**	6.53	18.0	23.4	13.1	330	**15510**

Notes: $^{(1)}$ Unit of N(H$_2$) is 10^{22} cm^{-2}

$^{(2)}$ This source was also observed in NH$_3$ by Sridharan et al. (2005), with a better signal-to-noise ratio. We therefore use the kinetic temperature derived by this study rather than our own data for this source.

$^{(3)}$ Only the (1,1) transition of NH$_3$ is detected at this position, so that no kinetic temperature could be derived. A temperature of 15 K has been assumed to compute masses and column density for this source.

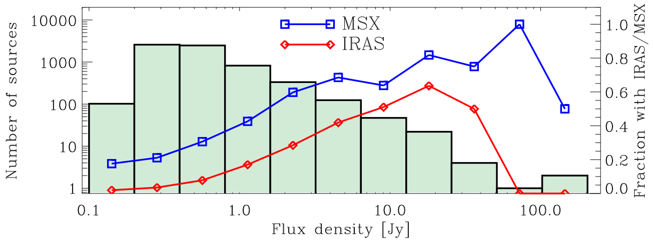

Fig. 12. Distribution of peak fluxes for the compact sources extracted in the data observed in 2007, shown in logarithmic scale. Fractions of sources associated with IRAS or MSX sources within a 30$''$ search radius are indicated, using the scale shown in the right hand side.

star-forming region, which harbors a giant Hii region. In most cases, the free-free emission accounts for ≤40% at 1.3 mm, one extreme case being where this fraction reaches 70%. Assuming a flat spectrum for free-free (optically thin case), and $F_\nu \propto \nu^{3.5}$ for the dust emission (i.e., a dust emissivity of $\beta = 1.5$), scaling from 240 GHz to 345 GHz implies that 20% of the flux originates from free-free emission at the LABOCA wavelength. In conclusion, the contribution from free-free should be almost negligible, and even in the most extreme cases should not exceed 20%.

4.4. Nature of the sources

Since dust emission in the submm is optically thin, the LABOCA observations are sensitive to all kinds of objects containing dust, which can range from cold, dense clumps within clouds to more evolved proto-stars that are centrally heated. We searched systematically for infrared counterparts to our preliminary catalog of 6000 sources in the IRAS Point Source Catalog (Beichman et al. 1988) and in the Midcourse Space Experiment (MSX, Price et al. 2001) data, using a search radius of 30$''$ (more details will be given in Contreras et al. in prep.). Only ∼10% of the submm compact sources can be associated with an IRAS point source, and ∼32% have a possible MSX counterpart (Fig. 12). In contrast, two thirds do not have a mid- or far-infrared counterpart in the IRAS/MSX catalogs, and could correspond to the coldest stage of star formation, prior to the birth of a massive proto-star. This fraction is similar to the results found by Motte et al. (2007) for the Cygnus-X region. However, with the superior sensitivity of the Spitzer GLIMPSE and MIPSGAL (Carey et al. 2005) surveys, weaker mid-IR sources are found to be associated with many of the MSX-dark, compact submm-clumps. Sources with IRAS associations generally correspond to later stages of star formation, e.g., hot molecular cores, compact Hii regions, or young embedded star clusters.

One should note that in some bright, complex star-forming regions, because of crowding and blending, even strong infrared sources do not fulfill the point-source selection criteria and, consequently, are not included in the IRAS/MSX catalogs. An extreme example is seen in the histogram of Fig. 12, where the brightest source in the survey, SgrB2(N), is counted as a source without IRAS/MSX association.

High-contrast IRDCs are easily identified by ATLASGAL. These clouds can have various shapes, from compact cores to filamentary morphologies of 1–5 arcmin in size. As an example,

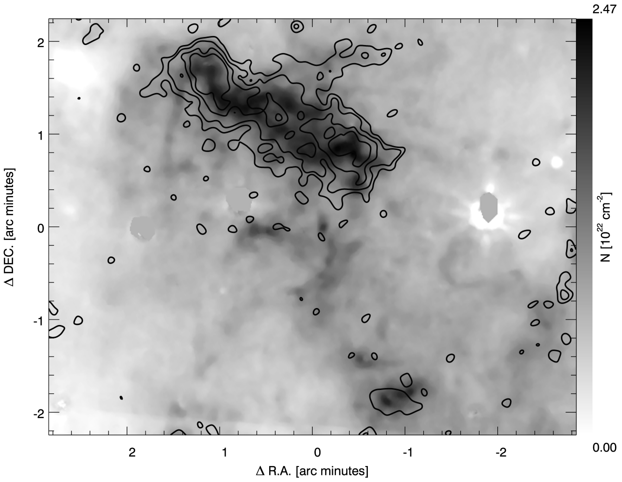

Fig. 13. Column density map of the IRDC G19.30+0.07, contained in the $l = 19°$ demonstration field. The map is derived from 8 μm extinction values measured in the corresponding Spitzer/GLIMPSE map. The ATLASGAL emission at 870 μm is overlaid in contours. The map center is at $\alpha = 18^h\,25^m\,53.94^s$, $\delta = -12°\,05'43.9''$ (J2000), or $l = 19.2771°$, $b = +0.0703°$.

our demonstration field contains the already well-investigated IRDC G19.30+0.07 (Carey et al. 1998). In Fig. 13, we show a column-density map of this IRDC, based on an extinction map derived from GLIMPSE 8 μm data. The $R_V = 5.5$ extinction law of Weingartner & Draine (2001) has been used. Further details of this approach are described in a forthcoming publication (Vasyunina et al. 2009). Overlaid as contours are the ATLASGAL 870 μm emission data. There is good agreement between the morphologies observed in both datasets, especially at the high column-density center of the IRDC. With an adopted distance of 2.38 kpc, roughly 260 $M_\odot$ are collected in this clump. IRDCs are considered to be a good hunting ground for the earliest phases of star formation, and ATLASGAL is expected to reveal a considerable fraction of them to be sub-mm emission sources.

Some sources seen in the submm may also correspond to *low-mass* star-forming sites located at small distances. However, our survey is sensitive to 1 $M_\odot$ dense clumps up to a distance of ~1 kpc only (Eq. (1)). In addition, nearby regions of star formation are likely to be located away from the Galactic Plane, outside the area covered by ATLASGAL. Therefore, low-mass star-forming clumps are not expected to be a dominant population in our data.

A small fraction of sources detected in the submm may not be related to star formation. These sources include late evolved stars with circumstellar envelopes, planetary nebulae, the nuclei of external galaxies, and quasars. However, we estimate that the contamination due to these classes of objects is negligible. For instance, following the method outlined by Anglada et al. (1998, Appendix), the number of background sources per arcmin^2 with flux densities at 5 GHz above S is:

$$N(arcmin^{-2}) = 0.011 \times S\,(mJy)^{-0.75} \qquad (4)$$

Assuming that the flux density scales with frequency as $S \propto \nu^{-0.7}$, one then obtains, for $\nu = 345$ GHz, 0.10 sources above 150 mJy per square degree, or about 10 background sources in the 95 deg^2 area discussed here. The extrapolation from 5 GHz to 345 GHz is quite uncertain, but this example illustrates nevertheless that the number of these background sources must be very low.

Another estimate can be derived from deep-field surveys in the submm. Integrating the differential source counts from the SCUBA Half-Degree Extragalactic Survey at 850 μm (SHADES, Coppin et al. 2006, their Eq. 12 and Table 7), yields 1×10^{-3} sources per square degree with flux densities above 150 mJy, or 0.1 sources above this limit in our surveyed area. Thus, we do not expect to detect any high-redshift object in our data.

The situation for late evolved stars may be more complex. As an example, the red supergiant VY CMa, which is one of the brightest sources at IR wavelengths and is at a distance of ~1.5 kpc, has a flux density of 1.5 Jy at 870 μm, as measured with LABOCA. Therefore, this object is detectable out to a distance of 3.5 kpc with our survey sensitivity. Less extreme or more distant objects of similar nature will most likely fall below our detection limits, but we cannot exclude having a small fraction of supergiants and extreme late evolved stars in our data. It will be possible to identify such objects from their colors at other wavelengths, e.g., in the Spitzer surveys (Robitaille et al. 2008).

5. Perspectives

5.1. An unbiased survey

This survey will provide the first unbiased database of Galactic sources at submm wavelengths, covering the inner 120° of the Galaxy in a systematic fashion. Since dust emission in the submm is optically thin, it is directly proportional to the mass of material (assuming a constant temperature) and leads to the detection of all proto-stellar objects or pre-stellar clumps and cores. With a 5-σ detection limit of 250 mJy/beam, this survey will be complete for proto-stellar cores down to ~10 $M_\odot$ at 2 kpc, or ~50 $M_\odot$ at 5 kpc (Fig. 11). In addition, the data will allow the investigation of the structure of molecular complexes on various scales, from their lower-intensity filaments to higher-density star-forming regions.

The systematic nature of this survey will also allow a complete census of extreme sources in the inner Galaxy, such as the high-mass star-forming regions W49 or W51. With our sensitivity, we should detect, at a 10-σ level, sources on the far side of the Galaxy, 25 kpc away, of masses as low as about 1500 $M_\odot$.

The unbiased nature of this database is critically important in compiling robust samples of objects for all types of follow-up projects based on a reliable statistical analysis. This is especially true in the context of ALMA (see also Sect. 5.5 below), which will explore exactly the same part of the sky as APEX in the (sub)mm range.

5.2. Evolutionary stages of high-mass star-formation

This database will contain a large number of high-mass clouds with submm emission not associated with developed star formation (as traced in the infrared surveys), which are expected to correspond to the earliest phases during the formation of the richest clusters of the Galaxy. Since high-mass proto-stars are rare (Motte et al. 2007), such large-scale surveys are required to obtain large samples of objects corresponding to the different stages of massive-star formation. Thus, the data will allow us to determine a basic evolutionary sequence for high-mass star formation.

Another topic that can be addressed with these data is the importance of triggered star formation, which can be assessed by identifying the second generation stars at the edges of HII regions (e.g., Deharveng et al. 2005) and supernova remnants. In the context of high-mass star formation in particular, the importance of triggering compared to spontaneous star formation remains an open question.

5.3. Distances and Galactic structure

Dust emission relates the star-forming regions seen in the IR/radio to the molecular clouds seen in CO, e.g., in the Galactic Ring Survey, by tracing the highest column-density features: compact sources and filaments. With the help of both extinction maps and absorption lines toward HII regions (Sewilo et al. 2004), the near/far ambiguity of kinematic distances can be solved in deriving the proper distances for a large fraction of ATLASGAL sources (Sect. 4.2). This will therefore help to improve our 3D view of the Galaxy. These data will also allow us to discover new coherent star-formation complexes up to distances of a few kpc. Finally, these data will allow us to compare the star-formation processes at different locations, in the spiral arms and inter-arm regions, and between the different arms.

5.4. Ancillary data

The region that we plan to map covers the same area as the GLIMPSE and MIPSGAL surveys (e.g., Fig. 14). It will also be mapped with PACS and SPIRE for the approved Hi-GAL (the Herschel infrared Galactic Plane Survey; Molinari et al.) open-time Herschel key project. The ATLASGAL data will thus be cross-correlated with similar large-scale Galactic surveys at other wavelengths, in the near- to far-infrared range, for example with the J, H, K UKIDSS Galactic Plane Survey (Lucas et al. 2008), providing spectral energy distributions from ~1 to 870 μm. The LABOCA data at 870 μm are crucial to estimating the total amount of dust along the line of sight. The combination of data from APEX, Spitzer, and Herschel will provide an extraordinary new database of the Galactic Plane from the near-IR to the millimeter, at a spatial resolution $\lesssim 30''$.

We will also correlate our data with existing radio surveys in the centimeter range: the NRAO VLA Sky Survey (NVSS, Condon et al. 1998), the Multi-Array Galactic Plane Imaging Survey (MAGPIS, Helfand et al. 2006), the Sydney University Molonglo Sky Survey (SUMSS, Mauch et al. 2003), and the Co-Ordinated Radio 'N' Infrared Survey for High-mass star formation (CORNISH)[1]. It will be of particular interest to compare with surveys of the radio continuum and maser emission that will be possible with the Expanded Very Large Array and the Australia Telescope Compact Array in the near future (Menten 2007). Existing or upcoming molecular-line databases include those resulting from the multi-beam CH_3OH maser Galactic Plane survey (Green et al. 2007) and from surveys, e.g., in the CS or ^{13}CO molecules (Bronfman et al. 1996; Urquhart et al. 2007). Combining ATLASGAL with the IR to cm data will allow us to establish a solid picture of the star-formation evolutionary stages and their associated timescales.

Several bolometer arrays are expected to be installed at APEX in the near future, including the Submillimetre APEX Bolometer Camera (SABOCA), a 37-element array observing at 350 μm, with a beam of 7.″7. Our team plans to complement the 870 μm data with targeted observations at 350 μm, covering limited areas of a few arcmin extent, to constrain the dust emissivity and resolve bright sources in crowded regions. The 870 μm survey might also be extended in surface area (toward the outer Galactic Plane), or to greater depth for a small part of the Galactic Plane (20 mJy/beam rms or less).

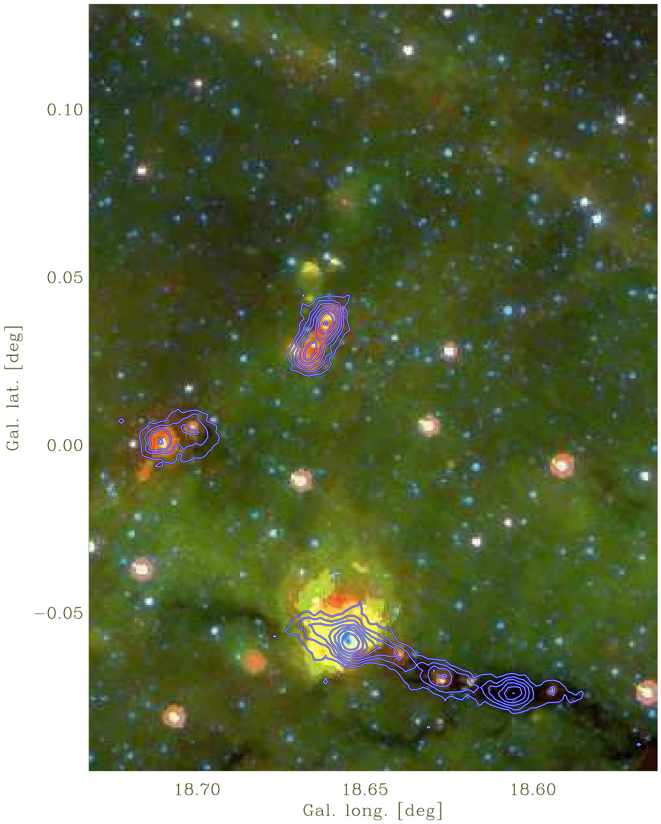

Fig. 14. Three-color image from Spitzer surveys: GLIMPSE 4.5 μm in blue (mostly tracing stars) and 8 μm in green (mostly PAH emission), MIPSGAL 24 μm in red, with 870 μm emission overlaid in contours.

A similar survey of the northern Galactic Plane ($l \geq -10°$) has started with the BOLOCAM instrument at the Caltech Submillimeter Observatory (CSO), at a wavelength of 1.1 mm (Drosback et al. 2008), with a $27''$ resolution. The northern Galactic Plane will also be mapped with the SCUBA-2 instrument at 450 and 850 μm, with resolutions of $8''$ and $15''$, respectively. In particular, as part of the SCUBA-2 "All-Sky" Survey (SASSY, Thompson et al. 2007), a 10° wide strip covering $|b| \leq 5°$ over the part of the Galactic Plane accessible from Hawaii will be observed at 850 μm with a one-σ sensitivity of 30 mJy/beam, comparable to the ATLASGAL survey. In addition, the JCMT Galactic Plane Survey plans to cover much deeper the area $+10° \leq l \leq +65°$, $|b| \leq 1°$, at both 450 and 850 μm. Combining data from these large-scale surveys will provide data at three different wavelengths in the Rayleigh-Jeans part of the dust emission spectrum, thus allowing us to study, among others, the dust emissivity, related to the composition of the dust.

5.5. Legacy value

The raw data will be available to outside users through the ESO archive[2] one year after the end of each observing period. We also plan to make the reduced combined maps available to the community; in addition, a compact-source catalog (including associations with surveys at other wavelengths) and a catalog of extended objects will be published upon completion. These will be available from a public web site[3]. This project will thus have a high legacy value, providing well characterized samples of targets to address in detail many questions of astrophysics. Calibrated maps built from the data observed in 2007 and discussed in the present paper are expected to be available online, both on the ESO archive and the ATLASGAL public website, by Summer 2009.

---

[1] `http://www.ast.leeds.ac.uk/Cornish/index.html`

[2] `http://archive.eso.org/wdb/wdb/eso/apex/form`

The observations that we have planned should be completed by the end of 2009, i.e. when the Herschel observatory is expected to deliver its first science data. Our team will be involved in the investigation of systematic associations between the ATLASGAL sources and Herschel products. In particular, members of the consortium are leading the key projects HOBYS (the Herschel imaging survey of OB Young Stellar objects; Motte, Zavagno, Bontemps et al.) and Hi-GAL.

The first ALMA antennas should also be available for early science soon after completion of our survey. This will be the perfect time for conducting follow-ups of carefully selected targets at an unprecedented spatial resolution. The ATLASGAL catalog will provide ALMA with more than 10^4 compact sources, including hot cores, high-mass proto-stellar objects, and cold pre-stellar cores. All sorts of molecular lines will be available to study the chemistry of the sources, or to search for signatures of infall or outflows for example. Thus, ATLASGAL is expected to trigger numerous follow-up studies to characterize the detected sources in terms of their excitation and chemistry. ATLASGAL will also provide the James Webb Space Telescope (JWST) with samples of well characterized targets, and these future facilities will allow one to study the inner workings of the star-formation process on small scales. This survey is therefore an essential pathfinder for Herschel, ALMA, and the JWST.

In addition to the new findings in the realm of high-mass star formation, the survey will tell us on a larger scale details about the structure and mass distribution in our Galaxy and help us to connect our knowledge of local star formation with star formation in external galaxies, where high-mass stars are the only ones that we see.

Acknowledgements. We thank the APEX staff for their help during the observations, and for their continuous support with LABOCA operations. This research has made use of the SIMBAD database, and of the Aladin Sky Atlas, both operated at CDS, Strasbourg, France. H.B. acknowledges financial support by the Emmy-Noether-Program of the Deutsche Forschungsgemeinschaft (DFG, grant BE2578). L.B., G.G., and D.M. acknowledge support from Chilean Center of Excellence in Astrophysics and Associated Technologies (PFB 06), and from Chilean Center for Astrophysics FONDAP 15010003.

References

Adams, F. C., Lada, C. J., & Shu, F. H. 1987, ApJ, 312, 788
Anderson, L. D. & Bania, T. M. 2009, ApJ, 690, 706
André, P., Ward-Thompson, D., & Barsony, M. 2000, Protostars and Planets IV, 59
Anglada, G., Villuendas, E., Estalella, R., et al. 1998, AJ, 116, 2953
Beichman, C. A., Neugebauer, G., Habing, H. J., Clegg, P. E., & Chester, T. J., eds. 1988, Infrared astronomical satellite (IRAS) catalogs and atlases. Volume 1: Explanatory supplement, Vol. 1
Benjamin, R. A., Churchwell, E., Babler, B. L., et al. 2003, PASP, 115, 953
Bertin, E. & Arnouts, S. 1996, A&AS, 117, 393
Beuther, H., Churchwell, E. B., McKee, C. F., & Tan, J. C. 2007, in Protostars and Planets V, ed. B. Reipurth, D. Jewitt, & K. Keil, 165–180
Beuther, H., Walsh, A., Schilke, P., et al. 2002, A&A, 390, 289
Bonnell, I. A., Vine, S. G., & Bate, M. R. 2004, MNRAS, 349, 735
Brand, J. & Blitz, L. 1993, A&A, 275, 67
Bronfman, L., Casassus, S., May, J., & Nyman, L.-Å. 2000, A&A, 358, 521
Bronfman, L., Nyman, L.-A., & May, J. 1996, A&AS, 115, 81
Carey, S. J., Clark, F. O., Egan, M. P., et al. 1998, ApJ, 508, 721
Carey, S. J., Noriega-Crespo, A., Price, S. D., et al. 2005, in Bulletin of the American Astronomical Society, Vol. 37, 1252
Condon, J. J., Cotton, W. D., Greisen, E. W., et al. 1998, AJ, 115, 1693
Coppin, K., Chapin, E. L., Mortier, A. M. J., et al. 2006, MNRAS, 372, 1621
Deharveng, L., Zavagno, A., & Caplan, J. 2005, A&A, 433, 565
Deharveng, L., Zavagno, A., Schuller, F., et al. 2009, A&A, 496, 177
Di Francesco, J., Johnstone, D., Kirk, H., MacKenzie, T., & Ledwosinska, E. 2008, ApJS, 175, 277
Dowell, C. D., Allen, C. A., Babu, R. S., et al. 2003, in Society of Photo-Optical Instrumentation Engineers (SPIE) Conference Series, ed. T. G. Phillips & J. Zmuidzinas, Vol. 4855, 73–87
Drosback, M. M., Aguirre, J., Bally, J., et al. 2008, in American Astronomical Society Meeting Abstracts, Vol. 212, 96.01
Enoch, M. L., Young, K. E., Glenn, J., et al. 2006, ApJ, 638, 293
Evans, II, N. J., Allen, L. E., Blake, G. A., et al. 2003, PASP, 115, 965
Faúndez, S., Bronfman, L., Garay, G., et al. 2004, A&A, 426, 97
Frerking, M. A., Langer, W. D., & Wilson, R. W. 1982, ApJ, 262, 590
Gahm, G. F., Lehtinen, K., Carlqvist, P., et al. 2002, A&A, 389, 577
Garay, G., Faúndez, S., Mardones, D., et al. 2004, ApJ, 610, 313
Green, J. A., Cohen, R. J., Caswell, J. L., et al. 2007, in IAU Symposium, Vol. 242, IAU Symposium, 218–222
Groesbeck, T. D. 1995, PhD thesis, California Institute of Technology.
Güsten, R., Booth, R. S., Cesarsky, C., et al. 2006a, in SPIE Conference, Vol. 6267, Ground-based and Airborne Telescopes. Edited by Stepp, Larry M.. Proceedings of the SPIE, Volume 6267, pp. 626714
Güsten, R., Nyman, L. Å., Schilke, P., et al. 2006b, A&A, 454, L13
Hatchell, J., Richer, J. S., Fuller, G. A., et al. 2005, A&A, 440, 151
Helfand, D. J., Becker, R. H., White, R. L., Fallon, A., & Tuttle, S. 2006, AJ, 131, 2525
Hildebrand, R. H. 1983, QJRAS, 24, 267
Hinz, J. L., Rieke, G. H., Yusef-Zadeh, F., et al. 2009, ApJS, 181, 227
Jackson, J. M., Rathborne, J. M., Shah, R. Y., et al. 2006, ApJS, 163, 145
Johnstone, D., Di Francesco, J., & Kirk, H. 2004, ApJ, 611, L45
Lucas, P. W., Hoare, M. G., Longmore, A., et al. 2008, MNRAS, 391, 136
Lumsden, S. L., Hoare, M. G., Oudmaijer, R. D., & Richards, D. 2002, MNRAS, 336, 621
Mac Low, M.-M. & Klessen, R. S. 2004, Reviews of Modern Physics, 76, 125
Mauch, T., Murphy, T., Buttery, H. J., et al. 2003, MNRAS, 342, 1117
McKee, C. F. & Ostriker, E. C. 2007, ARA&A, 45, 565
McKee, C. F. & Tan, J. C. 2002, Nature, 416, 59
McKee, C. F. & Tan, J. C. 2003, ApJ, 585, 850
Menten, K. M. 2007, in IAU Symposium, Vol. 242, Astrophysical Masers and their Environments, Proceedings of the IAU, 496–505
Menten, K. M., Pillai, T., & Wyrowski, F. 2005, in IAU Symposium, Vol. 227, Massive Star Birth: A Crossroads of Astrophysics, ed. R. Cesaroni, M. Felli, E. Churchwell, & M. Walmsley, 23–34
Molinari, S., Brand, J., Cesaroni, R., & Palla, F. 1996, A&A, 308, 573
Moore, T. J. T., Bretherton, D. E., Fujiyoshi, T., et al. 2007, MNRAS, 379, 663
Motte, F., Andre, P., & Neri, R. 1998, A&A, 336, 150
Motte, F., Bontemps, S., Schilke, P., et al. 2007, A&A, 476, 1243
Motte, F. & Hennebelle, P. 2009, in EAS Publications Series, ed. L. Pagani & M. Gerin, Vol. 34, 195–211
Motte, F., Schilke, P., & Lis, D. C. 2003, ApJ, 582, 277
Muders, D., Hafok, H., Wyrowski, F., et al. 2006, A&A, 454, L25
Ossenkopf, V. & Henning, T. 1994, A&A, 291, 943
Palla, F., Brand, J., Comoretto, G., Felli, M., & Cesaroni, R. 1991, A&A, 246, 249
Palla, F., Cesaroni, R., Brand, J., et al. 1993, A&A, 280, 599
Pestalozzi, M. R., Minier, V., & Booth, R. S. 2005, A&A, 432, 737
Price, S. D., Egan, M. P., Carey, S. J., Mizuno, D. R., & Kuchar, T. A. 2001, AJ, 121, 2819
Rathborne, J. M., Jackson, J. M., & Simon, R. 2006, ApJ, 641, 389
Robitaille, T. P., Meade, M. R., Babler, B. L., et al. 2008, AJ, 136, 2413
Schilke, P., Groesbeck, T. D., Blake, G. A., & Phillips, T. G. 1997, ApJS, 108, 301
Sewilo, M., Watson, C., Araya, E., et al. 2004, ApJS, 154, 553
Shu, F. H., Adams, F. C., & Lizano, S. 1987, ARA&A, 25, 23
Simon, R., Jackson, J. M., Rathborne, J. M., & Chambers, E. T. 2006, ApJ, 639, 227
Siringo, G., Kreysa, E., Kovács, A., et al. 2009, A&A, 497, 945
Siringo, G., Weiss, A., Kreysa, E., et al. 2007, The Messenger, 129, 2
Sridharan, T. K., Beuther, H., Saito, M., Wyrowski, F., & Schilke, P. 2005, ApJ, 634, L57
Sridharan, T. K., Beuther, H., Schilke, P., Menten, K. M., & Wyrowski, F. 2002, ApJ, 566, 931

---

[3] `http://www.mpifr-bonn.mpg.de/div/atlasgal/`

Thompson, M. A., Serjeant, S., Jenness, T., et al. 2007, astro-ph, 0704.3202
Urquhart, J. S., Busfield, A. L., Hoare, M. G., et al. 2007, A&A, 474, 891
Vasyunina, T., Linz, H., Henning, T., et al. 2009, A&A, accepted, astro-ph/0902.1772
Walsh, A. J., Hyland, A. R., Robinson, G., & Burton, M. G. 1997, MNRAS, 291, 261
Ward-Thompson, D., André, P., Crutcher, R., et al. 2007, in Protostars and Planets V, ed. B. Reipurth, D. Jewitt, & K. Keil, 33–46
Weingartner, J. C. & Draine, B. T. 2001, ApJ, 548, 296
Williams, J. P., Blitz, L., & McKee, C. F. 2000, Protostars and Planets IV, 97
Wood, D. O. S. & Churchwell, E. 1989, ApJ, 340, 265
Wyrowski, F. 2008, in Astronomical Society of the Pacific Conference Series, ed. H. Beuther, H. Linz, & T. Henning, Vol. 387, 3
Wyrowski, F., Menten, K. M., Schilke, P., et al. 2006, A&A, 454, L91
Young, K. E., Enoch, M. L., Evans, II, N. J., et al. 2006, ApJ, 644, 326
Zinnecker, H. & Yorke, H. W. 2007, ARA&A, 45, 481